

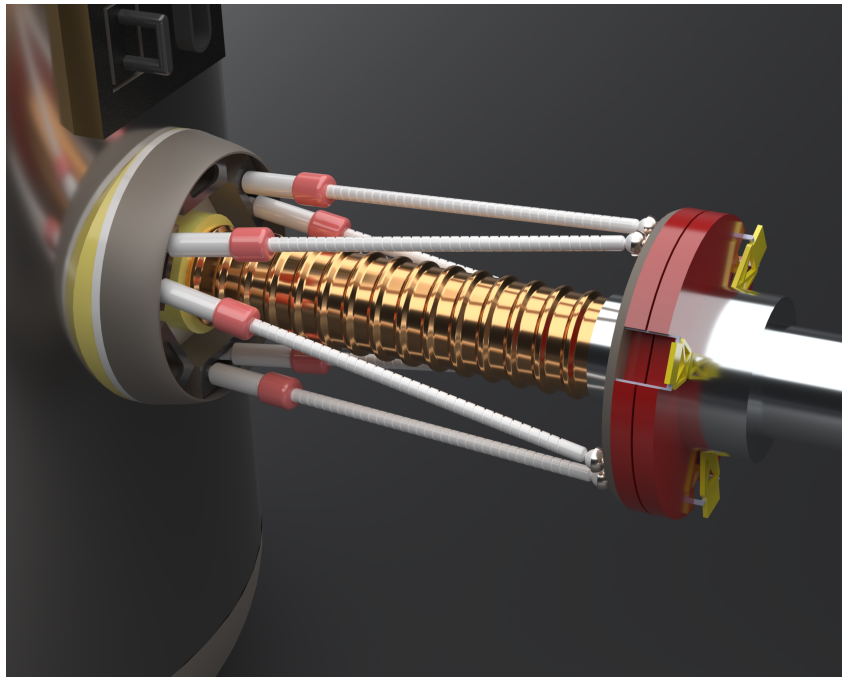
AMCC-AAC: Autonomous Magnetized Cryo-Couplers with Active Alignment Control for Propellant Transfer

2025 Human Lander Challenge (HuLC)

The Ohio State University

Max Heil (Undergraduate, Aerospace Engineering)
Zafar Shaik (Undergraduate, Aerospace Engineering)
Nishanth Kunchala (Undergraduate, Aerospace Engineering)
Will Rueter (Undergraduate, Aerospace Engineering)
Kevin Subin (Undergraduate, Aerospace Engineering)
Rahul Ravishankar (Undergraduate, Aerospace Engineering)
Anastasia Anikina (Undergraduate, Aerospace Engineering)
Ryan Endicott (Undergraduate, Aerospace Engineering)
Shiv Amin (Undergraduate, Aerospace Engineering)
Tejdeep Somi Reddy (Undergraduate, Aerospace Engineering)
Artur Leonel Machado Ulsenheimer (Undergraduate, Aerospace Engineering)

Advisor: Dr. John Horack



Contents

1	Executive Summary	2
2	Introduction	2
2.1	Cryogenic Challenges & Problem Statement	2
2.2	Background	2
3	Technology Concept and Approach	3
3.1	Main Assumptions	3
3.2	System Overview	3
4	Engineering Design and Analysis	4
4.1	Structural and Mechanical Design	4
4.1.1	Fluid Flow	4
4.1.2	Movement System Overview	4
4.1.3	Clamping	5
4.1.4	Locking Mechanism	6
4.1.5	Magnetic Quick Disconnect	7
4.2	AI Movement and Docking System	7
4.3	Manufacturing	9
4.3.1	Non-Destructive Testing and Validation	10
4.3.2	Prototyping and Iteration	10
4.3.3	Final Development and Assembly	10
4.4	Thermal Considerations	11
4.4.1	Simulation Geometry and Mesh	11
4.4.2	Material and Flow Conditions	11
4.4.3	Boundary Conditions and Heat Flux	11
4.4.4	Thermal Results and Boil-Off Prediction	11
4.4.5	Limitations and Future Enhancements	12
4.4.6	Thermal Insulation Using Multi-Layer Insulation (MLI)	12
4.5	Propellant Transfer Validation	13
5	Prototype	14
5.1	3D Printed Model	14
5.2	Stewart Platform	14
6	Technical Management	15
6.1	Risk Assessment and Mitigation	15
6.2	Project Timeline and Budget Estimate	15

1 Executive Summary

Cryogenic propellant transfer on-orbit is essential for sustained lunar exploration but remains a major technical hurdle. Cryogenic fluids, stored at approximately -196°C , can only be maintained for several hours with current technologies [1]. Our solution, AMCC-AAC, is a reusable cryogenic coupler that combines active robotic alignment with passive magnetic capture and AI-based visual docking to maximize fluid transfer. Modeled after ISS mating systems, the design achieves sub-centimeter precision using LiDAR and camera fusion. Thermal modeling and CFD simulations demonstrate structural integrity and low-leakage flow under realistic cryogenic conditions. The system includes a quick-disconnect mechanism for fault mitigation and is manufactured using Laser Powder Bed Fusion (LPBF). AMCC-AAC addresses NASA's need for low-risk, autonomous cryogenic infrastructure compatible with systems like Starship and Gateway. By increasing transfer reliability and eliminating manual docking procedures, our solution supports long-duration lunar operations and advances the Artemis program's goal of continued human presence on the Moon.

2 Introduction

2.1 Cryogenic Challenges & Problem Statement

With a renewed focus on sustained lunar exploration, advancing cryogenic propellant technologies is more crucial than ever. NASA's Artemis program and the Gateway lunar space station aim to enable long-term human presence on the Moon, but achieving this goal requires overcoming significant challenges in cryogenic systems [2]. The SpaceX Starship Human Landing System (HLS), responsible for transporting astronauts to the lunar surface, depends on cryogenics such as liquid oxygen (LOX) and liquid methane (LCH_4) to safely do so. However, the capabilities of current cryogenic systems are underdeveloped relative to the needs of the HLS architecture. Addressing this issue requires novel, innovative solutions to ensure the long-term viability of lunar operations and deep-space exploration.

To bridge this technological gap, advancements in Cryogenic Fluid Management (CFM) are essential. CFM is a complex suite of technologies developed by the Space Technology Mission Directorate (STMD) to demonstrate the ability to successfully and adequately store, transfer, and measure cryogenic fluids in space [3]. One specific area of focus in CFM is large-scale autonomous on-orbit propellant transfer. Designing such a system poses unique challenges due to the behavior of cryogenic fluids in microgravity, including fluid sloshing, phase changes, and thermal management issues.

Ensuring reliable and autonomous cryogenic propellant transfer in space requires advancements in sealing technology, flow control, and thermal insulation to prevent losses from leakage and boil-off. Traditional quick-disconnect cryo-couplers, designed for ground-based applications, face significant challenges in the space environment. High sealing friction, wear-induced leakage, and limited reusability are among the most notable [4]. Additionally, existing couplers require precise manual alignment, making them impractical for automated docking in microgravity. To overcome these challenges, next-generation cryo-couplers must incorporate automation, improved sealing mechanisms, and materials engineered for cryogenic durability.

2.2 Background

Although cryogenic propellants such as LOX, LH_2 , and LCH_4 have been commonplace in expendable upper-stage launch vehicle operations for decades, no spacecraft has yet executed a closed-loop cryogenic propellant transfer in microgravity. The field is instead defined by recent component-level demonstrations and ground testing campaigns.

NASA's CFM roadmap identifies four critical functions that must reach TRL-6 before operational depots are feasible: (1) microgravity mass gauging, (2) high-efficiency tank-to-tank transfer, (3) long-duration low boil-off storage, and (4) controlled propellant acquisition devices (such as liquid acquisition devices/propellant management devices) [5, 6].

In addition to these subsystems, there remains a major integration challenge surrounding the development of an autonomous cryogenic coupler capable of supporting repeated operations in space. Prior technology assessments have emphasized the need for vapor-free liquid outflow, precise thermal conditioning for non-vented fill (NVF) operations, and reliable disconnection mechanisms for in-space

applications [5]. While extensive research has been conducted to understand NVF behavior, including chill-and-fill cycles and disconnection behavior, these findings are based on 1g testing environments and do not fully capture the challenges of propellant management in microgravity [7].

The most flight-representative experiment to date, NASA's Robotic Refueling Mission 3 (RRM3), launched to the International Space Station in December 2018. This demonstrated several key CFM capabilities including zero-boil-off storage of cryogenic methane, radio-frequency mass gauging, and autogenous pressurization [8]. However, due to an electronics anomaly, the mission was unable to complete the planned cryogenic transfer or liquid orientation experiments for full mission duration. As a result, despite a promising subsystem performance, a fully integrated and operational cryogenic transfer system has yet to be achieved in the space environment.

Together, these challenges point to a critical unmet need: the development of an autonomous cryogenic fuel transfer system with robust mechanical docking.

3 Technology Concept and Approach

3.1 Main Assumptions

Before we can give a detailed technical plan for creating an autonomous cryo-coupler system, we first must make some reasonable simplifying assumptions. These assumptions aim to make this project both realistic and flexible for future adaptation. First, we must assume that the HLS architecture follows a 1-stage design for descent and ascent. The descent stage will transfer the crew and cargo from Gateway orbit to the lunar surface and the ascent stage will return the crew and collected lunar samples from the lunar surface back to Gateway [9]. Additionally, we assume no more than 4 crew members will be transferred on the HLS [10]. This will become important when calculating the propellant mass transfer necessary for the mission.

We also assume that propellant transfer occurs between two spacecraft or tanks to maximize the system's applicability. For this project, we have selected the SpaceX Starship HLS as the refueling vehicle, meaning the interface must accommodate its round tank geometry [11]. To keep the project scope focused, we assume that propellant flow through the coupler is managed by a separate subsystem (i.e. pressure differential, pump, or tank venting system). While fluid transfer is a critical aspect, our design is specifically concerned with ensuring a precise and reliable mechanical connection between the two tanks in space.

Additionally, we assume that one tank remains stationary with a fixed-length receiving hose, while the other incorporates a movement system with a variable hose length for alignment. Our design also presumes that Starship has already docked with the receiving spacecraft or tanker, allowing us to concentrate solely on the automation of the coupling mechanism.

3.2 System Overview

To enhance CFM capabilities and develop a framework for reusable cryo-couplers in orbit, we propose an autonomous AI-driven active alignment system, integrated with passive magnetic alignment, to enable the safe and reliable transfer of large quantities of propellant to the HLS. AMCC-AAC aims to accomplish the following key objectives:

1. *Achieve repeatable autonomous docking* of the dynamic coupler with a stationary receiver by using both active and passive alignment.
2. *Reduce leakage and boil-off losses* while transferring large quantities of propellant by use of multilayer insulation (MLI), compressive robotic grippers, and advance o-ring sealants.
3. *Enable rapid emergency disconnect* via a magnetic-assisted quick release mechanism to prevent propellant loss and catastrophic damage.

We accomplish these objectives through use of LiDAR, cameras, onboard HLS sensors, and AI algorithms for sensor fusion and interpretation. Figure 1 provides a high level system overview flowchart of the automated alignment process. Once properly connected, several system checks are performed, and other necessary systems—such as power and communications—are linked before transferring fluid.

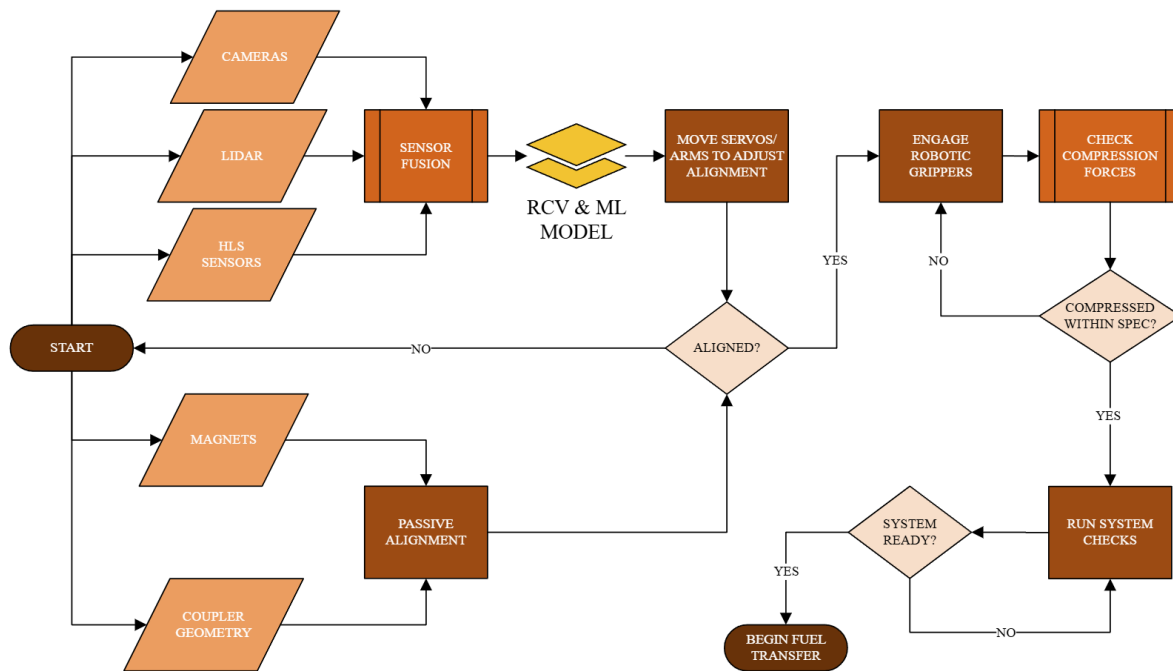


Figure 1: High Level System Overview Flowchart

The emergency disconnect system is a separately developed sub-process that will be integrated with a fluid transfer flowchart. This subsystem will be discussed in more detail below.

4 Engineering Design and Analysis

4.1 Structural and Mechanical Design

Microgravity and orbital alignment provide challenges that are important to consider when attempting to solve cryogenic fluid transfer. The design of the automated cryo-coupler utilizes several passive and active techniques, as well as specific design considerations to ensure a leak-free seal.

AMCC-AAC's design is broken down into several key components: internal fluid flow design, movement system, sealing and clamping, and coupler mating locks. Using specific NASA-based or industry-based standards, mock-ups for each section were created in SolidWorks and given quantifiable metrics and performance expectations. The design is discussed in detail in the following subsections.

4.1.1 Fluid Flow

While obvious, an important component we must consider when discussing cryogenic fluid transfer is the mass flow rate we expect from our design. Achieving the goal of repeatable and reliable cryogenic fluid transfer calls for the reduction of static pressure as much as possible within the system's constraints. Specifically, the coupler needs to be able to handle up to 25 kg/s for 12 hours based on the total ΔV of 5,400 m/s and mass requirements of 865kg (descent) & 525kg (ascent) for the planned Artemis missions (not including LEO to NRHO where $\Delta V \approx 9,355$ m/s) [9, 10, 12]. For this reason, an inner diameter of 5 inches has been chosen to accommodate a high mass-flow, low pressure fluid transfer. High mass flow leads to a reduction of lead times and subsequently decreases the risk of leaks. This diameter also allows for cross compatibility with existing plumbing hardware. A finalized section view of the AMCC-AAC CAD is shown in Fig. 2.

4.1.2 Movement System Overview

After both orbital bodies have approached, establishing the connection between both halves of the coupling is done by robotic movement rods using LiDAR and camera

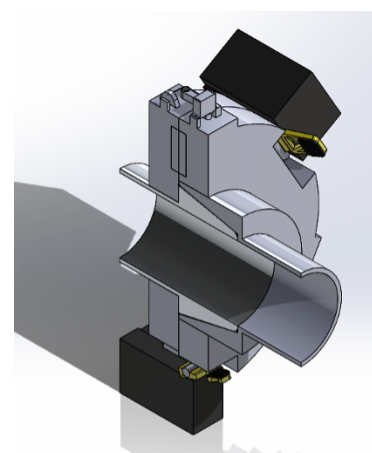


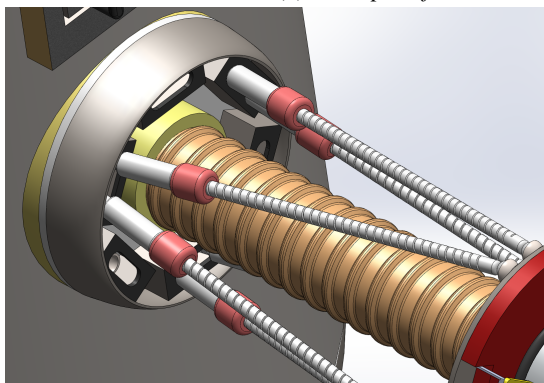
Figure 2: Nozzle Section View

data. The actuation system was modeled based off the ISS Block 1 Docking System illustrated in Fig. 3a. Similar to this system, our design uses a direct-drive electromechanical Stewart Platform-based capture system with six independent linear actuators to guide and align the couplers. The plate connection points have been modeled as ball bearings with the option to add more complex joints in the future. The movement system was designed so that it can be retracted into the conical holder until it is needed. A base plate will need to be added to the Starship HLS outer structure that conforms to its shape. However, the system was designed to only be additive rather than subtractive in terms of parts. No additional components of Starship HLS are compromised by the addition of the AMCC-AAC. The holder contains each of the robotic arms when in the stowed configuration. An example of the movement system fully extended and in a stowed configuration are provided in Fig. 3. Note that the length of the actuators and rods are exaggerated in this concept to better illustrate the detail in each component.

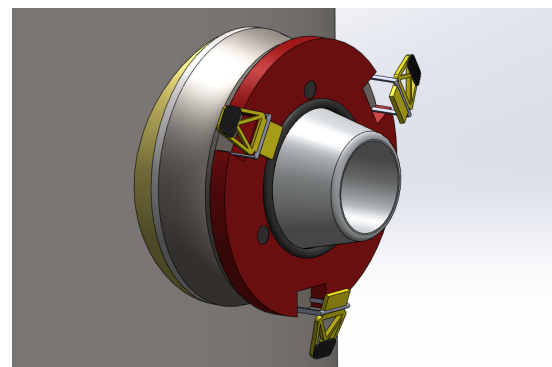
Within about 1 inch of mating, the magnets arranged in a radial pattern around each end of the coupling assist both in completing the rest of the displacement and in reinforcing the proper rotation to successfully mate the structure [13]. The angled walls of the nipple and sleeve will accommodate for any micro adjustments needed to guide the couplers into the proper position [14]. The specifics of this system are discussed in greater detail in a later section, due to its importance to this project.



(a) Example of ISS Docking System, Image Credit: NASA [15]



(b) Movement System Extended



(c) Stowed Movement System

Figure 3: The Attachment Plate to HLS with A Extended and Stowed Views

4.1.3 Clamping

Once in a mated position, 3 servo arms arranged equal radial distances automatically clamp down and secure the connection with 7.5 kN of force each. Based on an assumed maximum operating pressure of 1 MPa and a 5 in internal diameter, we expect an axial separation load defined by,

$$F_p = P_{max}A_{eff} = (1 \text{ MPa})(\pi D^2/4) \approx 12.7 \text{ kN} \quad (1)$$

where P_{max} is the maximum operating pressure and A_{eff} is the effective pressure area. Designing for a safety factor of 1.5 – 2.0, we arrive at the required clamping force for sealing the coupler effectively.

$$F_{req} = (F_p)(SF) \approx 20 - 25 \text{ kN} \quad (2)$$

By adding this axial force, the walls of the coupling will reach a minimum tolerance of 0.5mm and the o-ring sitting at the base will be fully engaged, creating a virtually leak-proof seal [16]. The 100 mm clamping arms require a servo that can torque up to 750 Nm, based on the axial force required. Therefore a flight capable actuator that can operate within the margins discussed would be the Moog M-Series Space Rotary Actuators [17]. While specific dimensions and torque specifications of this unit are unavailable publicly, it is likely that multiple actuators will be needed for a single clamping subsystem. Thus, a 5 in by 4 in box has been modeled near the yellow clamps to account for actuator storage and wiring. This is demonstrated in Figure 4.

4.1.4 Locking Mechanism

Sealing the mated ends together requires maintaining the precise alignment achieved by the movement system. Using the exact International Docking System Standard (IDSS) hooks proves to be applicable for this project. There are 3 hooking locations with 2 hooks at each point (1 passive and 1 active), each spaced radially 120° from one another. Under nominal loads and autonomous operating conditions, the active hooks engage with the passive hooks once contact is made. As shown in Figure 5a, the wiring and servos needed to operate the active hooks is modeled by a small 0.5 in by 1 in box. Figure 5b depicts the active hooks with a spring attachments while the passive hooks remain stationary. The hooks protrude approximately 0.7 in beyond the couplers interface, modeled exactly according to the Interface Definition Document (IDD) within IDSS (shown in Fig. 6) [18].

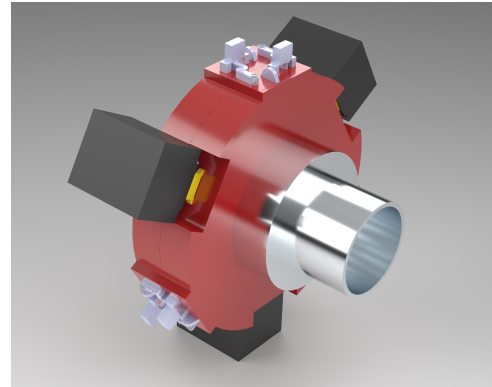
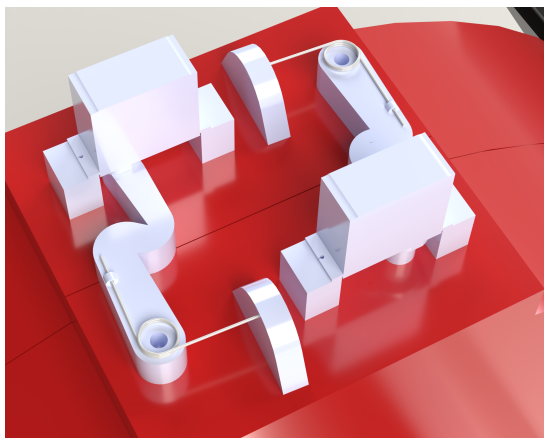
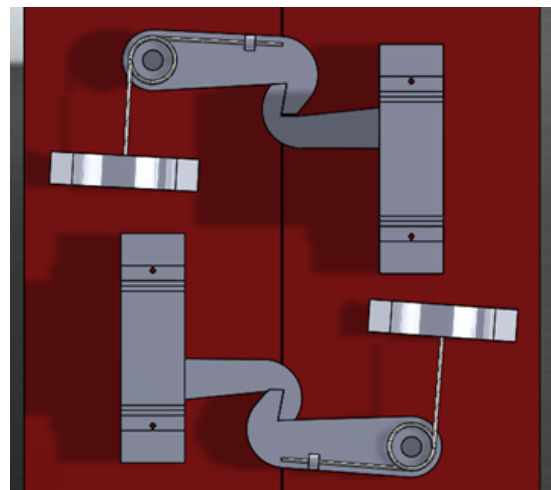


Figure 4: *Clamp Actuators Modeled by Black Box*



(a) *Locking Mechanism in Locked Position*



(b) *Active Hooks with Spring Attachments*

Figure 5: *Locking Mechanism Subsystem*

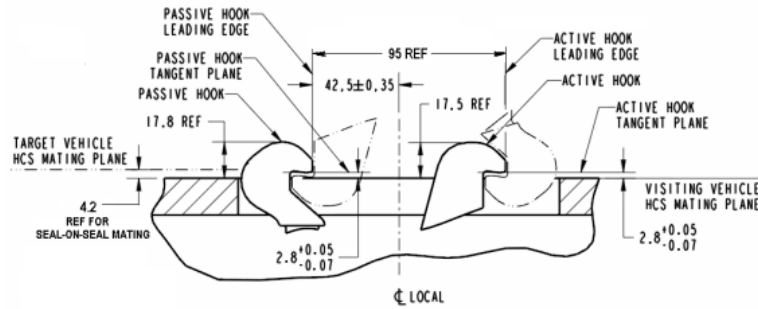


Figure 6: Ready to Hook Configuration of IDSS Hooks; Image Credit: NASA [18]

The hooks are designed with a load capacity of 50,000 N when locked [18]. This is well within the limitations of AMCC-AAC and provides ample room for error mitigation. To guarantee reliable performance throughout the coupler's service life, each active hook integrates a Hall-effect position switch that verifies the fully latched state while the drive electronics are cross-strapped to survive any single-point failure. In the event of an abort, the hooks can be commanded to the stowed position in under one second, after which the Stewart-platform actuators and passive magnets retract the coupler halves without imparting harmful side loads on the seal. Qualification of the locking subsystem is considered complete as this is a TRL-9 system aboard the ISS and many orbiters.

4.1.5 Magnetic Quick Disconnect

The coupler emergency disconnect is modeled after the Low Force Disconnect (LFD) system used in the CryoMag at Armstrong Flight Research Center. This system uses equal and opposite load forces applied by the o-ring pressure seals to result in a net zero separation force [19]. Our design implements a similar concept where the low engagement force is easily separated by use of o-rings and retraction of the electromechanical actuators on the movement system.

Six pairs of N52-grade neodymium ring magnets ($\varnothing 20 \text{ mm} \times 5 \text{ mm}$) are embedded symmetrically around the 5 in fluid passage. For two magnets aligned face-to-face at zero gap, the attractive load can be approximated by the magnetic pressure relation

$$F = \frac{B^2 A}{2\mu_0}, \quad (3)$$

where $B \approx 0.55 \text{ T}$ is the surface flux density, A is the pole-face area, and μ_0 is the permeability of free space. This yields $F_{\text{pair}} \approx 31 \text{ N}$; six pairs therefore supply $\sim 185 \text{ N}$ of symmetric preload, which is enough to maintain seal compression after the Stewart-platform actuators retract, yet low enough that the disconnect sequence can be driven by 50 N per actuator [20]. NdFeB magnets retain $> 90\%$ of their room-temperature magnetization at 90 K, and their remanence actually increases slightly as temperature falls, providing a comfortable margin at LOX/LCH₄ conditions [21].

In an emergency, the system's linear actuators extend by 3 mm to lift the O-ring seals out of contact. Because the LFD-inspired design balances internal pressure with seal force, only the magnetic preload must be overcome during separation. Each actuator produces about 60 N of axial force which is more than sufficient to overcome the 31 N load from each magnet pair. Within 150 ms, the magnets are far enough apart that their force drops significantly, allowing elastic energy in the flexures to complete the separation. A spring-loaded valve vents any trapped cryogenic fluid safely away from the interface.

4.2 AI Movement and Docking System

We propose a modular vision-based navigation system to enable precise autonomous orbital refueling across spacecraft platforms such as SpaceX's Starship and NASA's Lunar Gateway. This system fuses computer vision, fiducial tracking, and range sensing through a two-stage Kalman filter to achieve sub-centimeter pose accuracy in the space environment. It integrates machine learning with interpretable geometric inputs to ensure robust performance in low-visibility and high-risk docking scenarios.

Originally developed for 2D keypoint detection of the ISS docking port, our AI model is being extended to 3D by incorporating depth data and transitioning from a modified MobileNetV3Small CNN to a Multi-Head Network (MHN). This upgrade allows direct regression of 3D coordinates, increasing spatial awareness and accuracy during cryogenic coupling. An example of the original 2D model's output is shown in Fig. 7.

This approach aligns with recent advancements in keypoint detection for space applications, where high-resolution networks and online keypoint mining techniques have demonstrated improvements in pose estimation accuracy, particularly in low-visibility conditions [22]. Docking and cryogenic coupling share fundamental requirements, such as precise alignment, secure engagement, and real-time decision-making. Due to these similarities, we pose that our model can be adapted for cryogenic coupling systems.

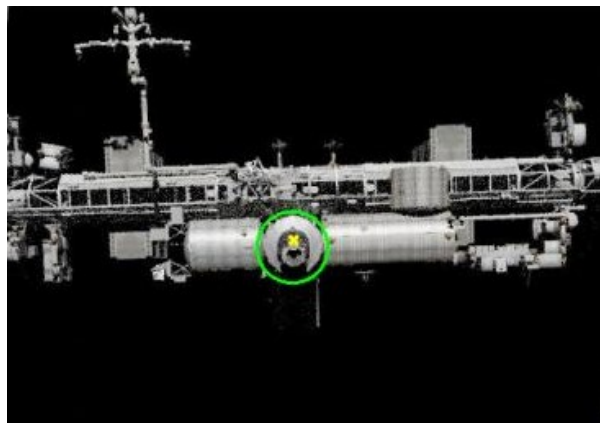


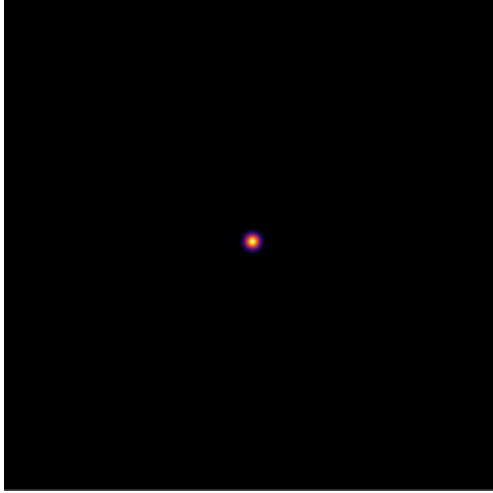
Figure 7: 2D Keypoint of ISS Port Identification Showing Accuracy w/ Clear Image

The two-stage Kalman filter architecture enables real-time fusion of vision and depth sensors. In the primary stage, pose estimates are generated from AI-based heatmaps and AprilTag fiducials. The AI-based computer vision component utilizes a deep learning model trained on 10,000 labeled images, each standardized to 512×512 pixel resolution. The model outputs a heatmap indicating the estimated docking port position on the image plane, with the width of the heatmap peak serving as a confidence metric. Narrow, focused peaks indicate high-confidence detections and receive full weight in the sensor fusion process, while broad or multi-modal peaks suggest uncertainty and are down-weighted accordingly. This confidence assessment allows the system to adapt its reliance on AI predictions based on the quality and certainty of the detection. Figure 8 demonstrates what a high and low confidence heatmap might look like. In the secondary stage, LiDAR range measurements refine translational estimates and serve as fallback when visual tracking degrades.

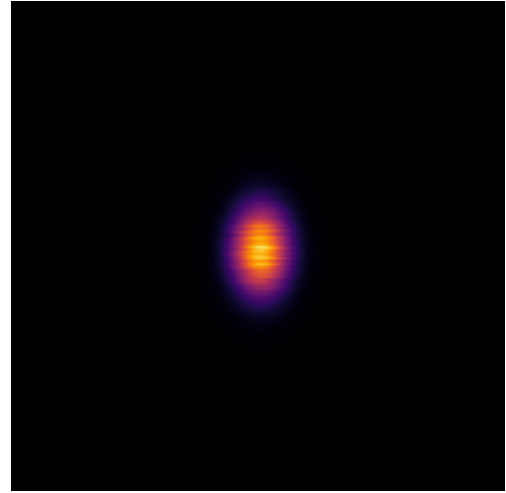
The AprilTag system complements the AI component by providing deterministic pose estimates and acting as a cross-check to mitigate false detections. Strategic placement ensures at least one tag remains visible despite occlusion, and redundancy across multiple tags improves accuracy. Figure 9 shows predicted RMS pose error versus AprilTag count and AI confidence. A docking attempt proceeds only when this error falls below the 5 cm threshold.

If all sensor confidences fall below threshold, the system initiates an automatic repositioning maneuver to improve visibility before reattempting docking. This low-confidence abort protocol ensures safety by avoiding risky engagements under poor visual conditions.

The final docking capture is completed by the magnetic coupling system (Section 4.1.5), which uses six pairs of $\text{Ø} 20 \text{ mm} \times 5 \text{ mm}$ N52-grade neodymium magnets embedded around the port. These generate an attractive force of approximately 31.3 N per pair (Eq. 3), enough to align couplers with residual misalignments under 5 cm and angular offsets below 15° . This 6-DOF correction relaxes precision demands on the vision system, allowing it to focus on coarse alignment within the magnetic capture envelope.



(a) *High-Confidence Heatmap Prediction (sharp, symmetric)*



(b) *Low-Confidence Heatmap Prediction (broad, irregular spread)*

Figure 8: *CNN Heatmap Confidence Examples*

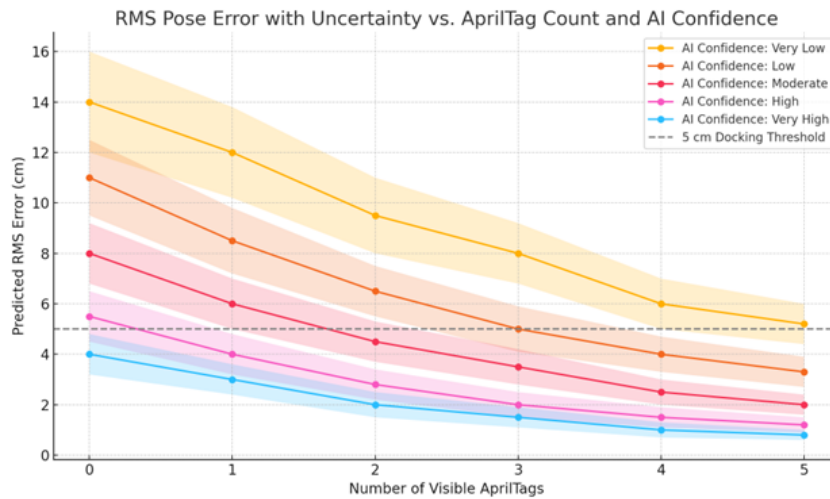


Figure 9: *Predicted RMS Pose Error vs AprilTag Count and AI Confidence. The Dashed Line Marks the 5 cm Docking Threshold.*

The system assumes uniform lighting via onboard sources and near-zero inertial relative velocity during coupling. These constraints simplify the computer vision task and enable the AI model to generalize across various scenarios.

From a computational standpoint, the model currently runs at 80–1000 ms per frame on an M1 CPU. Edge-AI accelerators and flight-ready GPUs offer 5× to 20× speed improvements [23], making real-time inference feasible for platforms like Starship HLS [24, 25].

Validation will progress from simulation to hardware-in-the-loop testing in cryogenic vacuum conditions. This staged approach aligns with NASA’s HLS verification guidelines [26] and ensures that the navigation system meets the safety and reliability standards required for autonomous, crew-adjacent operations.

4.3 Manufacturing

The cryogenic coupler will be fabricated using Laser Powder Bed Fusion (LPBF), an advanced additive manufacturing (AM) process optimized for high-precision aerospace components. LPBF enables the construction of complex internal geometries, topology-optimized structures, and integrated features

with minimal material waste. This process also reduces part count and facilitates design features not feasible with traditional subtractive machining.

Two materials are considered based on their cryogenic performance and structural demands. The initial development uses AlSi10Mg due to its high strength-to-weight ratio, excellent thermal conductivity, and demonstrated mechanical integrity at cryogenic temperatures [27]. However, for the final flight-ready production, Ti-6Al-4V (Grade 5) is selected due to its superior fatigue strength, corrosion resistance, and significantly lower coefficient of thermal expansion (CTE), which minimizes thermal mismatch and stress during repeated cryogenic cycling. Ti-6Al-4V is also highly compatible with deflection-actuated and metal-to-metal sealing technologies, making it ideal for propellant line couplings in high-vacuum environments.

The LPBF process begins with CAD optimization, emphasizing proper orientation for sealing surface quality, reduced support structure, and minimal post-processing. Fabrication occurs under an inert argon atmosphere to mitigate oxidation and ensure powder quality. Following the build, components undergo hot isostatic pressing (HIP) and heat treatment to relieve internal stresses, enhance mechanical durability, and eliminate porosity. For sealing-critical regions and interface zones, CNC machining is applied to achieve surface roughness below $R_a < 0.8 \mu\text{m}$, a critical threshold for reliable sealing. This hybrid manufacturing approach—LPBF followed by precision machining—leverages the design flexibility of additive processes and the surface finish precision of conventional techniques.

Table 1: Bill of Materials for Full-Scale Cryogenic Coupler

Component	Material	Quantity	Estimated Unit Cost
Main Housing	Ti-6Al-4V Powder	1	\$450/kg
Quick Disconnect Latch Assembly	Ti-6Al-4V	1	—
Seal Interface Surface Inserts	Ti-6Al-4V	1 set	\$150
Cryogenic Metal Seal	Inconel/X-750	1	\$90
Assembly Fasteners (Hex socket)	Ti Grade 2	6 pcs	\$4/pcs
Heat Treatment & HIP Processing	Service Cost	—	\$200
CNC Machining (Surface Finish)	Service Cost	—	\$250
NDT (X-ray or CT Scan)	Service Cost	—	\$300

4.3.1 Non-Destructive Testing and Validation

Structural integrity is confirmed via non-destructive testing (NDT) methods, including X-ray computed tomography (XCT) and dye penetrant inspection, to detect internal voids or structural flaws [28, 29]. Final sealing verification includes helium leak testing under simulated cryogenic conditions to ensure the coupler meets NASA’s performance standards for long-duration in-space cryogenic fluid transfer [30, 31].

4.3.2 Prototyping and Iteration

Prior to metal fabrication, a polymer prototype is constructed using FDM-based 3D printing. Materials such as PLA and ABS validate rigid component fit and form, while TPU is used for flexible interface segments. This phase allows ergonomic testing of the latch mechanism and interface tolerances. The same CAD model is adapted for polymer slicing to ensure consistency between prototype and final hardware. A full 3D printed prototype is discussed in a later section.

4.3.3 Final Development and Assembly

Post-processing and machining services are sourced from in-house capabilities or external partners such as The Ohio State University’s Center for Design and Manufacturing Excellence (CDME) or B&G Tooling. CDME’s established vendor network ensures reliable sourcing of aerospace-grade Ti-6Al-4V and AlSi10Mg powders. Design analysis of the quick disconnect evaluates latching loads, thermal expansion tolerances, and reusability to ensure mechanical reliability in extreme lunar conditions.

Subscale metal prototypes will be iteratively tested for mechanical robustness, sealing performance, and quick-disconnect functionality. The system will undergo full-cycle validation in accordance with

NASA's TRL framework to achieve mission readiness for lunar refueling operations.

4.4 Thermal Considerations

To ensure the structural integrity and functionality of spacecraft components in temperatures ranging from 400K to 50K, a comprehensive thermal management strategy was implemented [32]. A detailed thermal simulation of the cryogenic coupler pipe was performed using ANSYS Thermal Desktop to model the temperature distribution, heat transfer, and boil-off rates due to external radiation. The goal was to evaluate insulation needs and minimize fluid losses due to boil-off under simulated lunar orbital conditions.

4.4.1 Simulation Geometry and Mesh

A cylindrical pipe geometry representing the cryogenic fluid path was modeled with an inner diameter of 0.127 m and an outer diameter of 0.1778 m. The mesh consisted of structured cells with a maximum cell size of 0.007 m in the solid domain and 0.005 m in the fluid domain. Inflation layers were included in both domains to accurately capture heat transfer across the fluid-solid interface.

4.4.2 Material and Flow Conditions

The simulation used Ti-6Al-2Sn-2Zr-2Mo-annealed titanium alloy for the pipe wall due to its thermal durability and oxygen compatibility. Liquid and gaseous oxygen phases were simulated in the fluid domain using the Lee model to approximate vaporization and boil-off effects. The flow was modeled as laminar, entering at 100 m/s and 90.15 K. An energy equation-based solver captured temperature gradients through the domain.

4.4.3 Boundary Conditions and Heat Flux

Solar radiation was modeled as a uniform heat flux of 1368 W/m^2 applied to the outer wall, consistent with lunar sun exposure conditions. Due to time limitations, the full radiation model in Thermal Desktop was not used. Microgravity effects were also neglected. Transient simulations were run for time steps of 20 and 25 iterations to capture boil-off onset, followed by steady-state runs for long-term behavior.

4.4.4 Thermal Results and Boil-Off Prediction

Figure 10 shows temperature gradients across both solid and fluid domains, highlighting the thermal diffusion through the wall. Figure 11 isolates the fluid domain, while Figure 12 illustrates vapor generation via oxygen volume fraction.

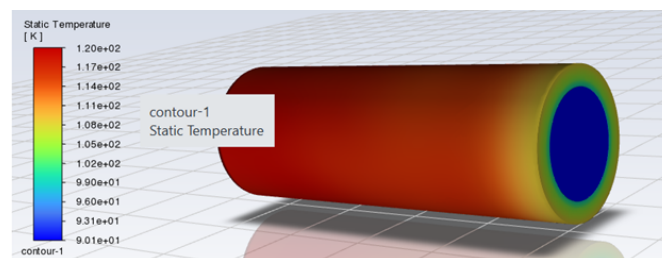


Figure 10: Static Temperature Distribution in Both Solid and Fluid Domains

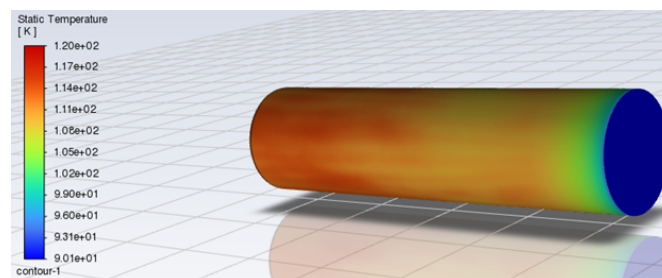


Figure 11: Static Temperature Distribution in Fluid Domain Only

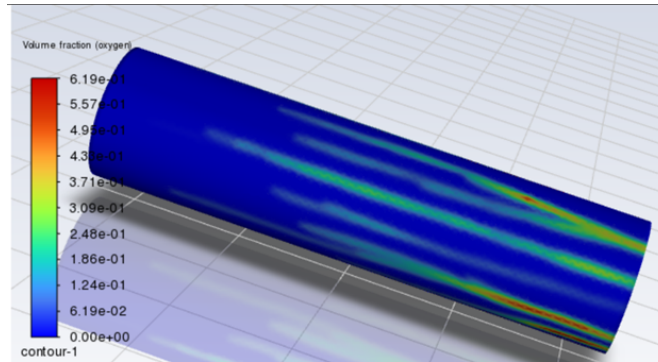


Figure 12: Volume Fraction of Oxygen (Gas Phase) Showing Boil-Off Regions

4.4.5 Limitations and Future Enhancements

Although the current approach offers useful insight into insulation requirements and thermal behavior, future refinements should include directionally dependent radiation models, implementation of the modified Dittus-Boelter correlation for improved convective modeling, and full gravity vector inclusion to model orbital or lunar surface conditions more accurately. Validation against ground-based cryogenic test data is also recommended to confirm predicted boil-off rates under operational conditions.

4.4.6 Thermal Insulation Using Multi-Layer Insulation (MLI)

To mitigate boil-off and minimize solar heating, several insulation materials were considered for both the prototype and flight versions of the AMCC-AAC system. For the prototype, the team selected cost-effective, commercially available materials that mimic NASA-grade MLI. One solution used metalized Mylar film with reflective bubble wrap, offering a low-emissivity outer surface and internal flexibility. This configuration costs approximately \$25 per meter and provides decent thermal protection for early-stage testing.

Another prototyping material, Reflectix, is a foil-faced polyethylene insulation that is easy to apply and wrap. Although not intended for vacuum environments, it performs well as a thermal barrier in atmospheric conditions, making it suitable for ground tests. Kapton tape was also used to seal edges and provide additional thermal protection, offering higher temperature resistance than Mylar and improved durability.

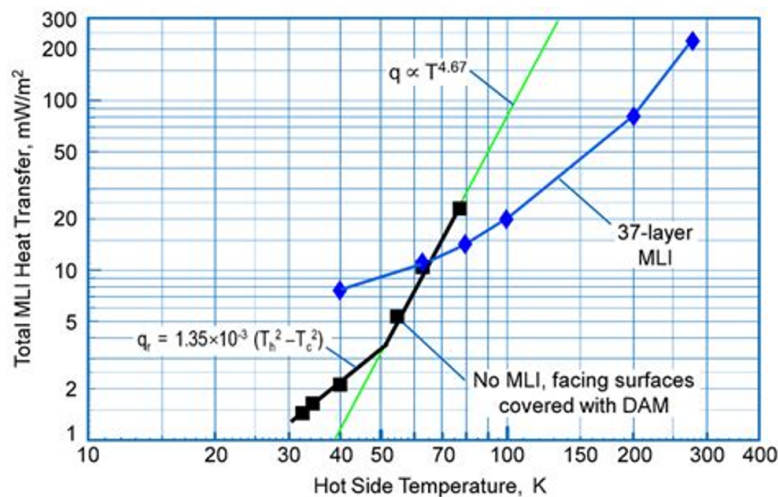


Figure 13: Measured Heat Transfer of 37-layer MLI Under Varying Conditions [33].

For a flight-ready system, space-qualified MLI would be required. The outermost layer would consist of aluminized Kapton (polyimide) due to its durability, high temperature tolerance (-269 to 400°C), and suitability for vacuum environments [34]. Beneath this, the stack would alternate layers of alu-

minimized Mylar, Dacron mesh, and Nomex felt spacers to minimize radiative and conductive heat transfer [33]. NASA MLI systems often include 10–30 such layers, achieving effective emissivity values as low as 0.005 in vacuum.

If externally mounted on a spacecraft, an additional Beta cloth outer cover (Teflon-coated fiberglass) would shield the system from micrometeoroids and add fire resistance [35]. This robust configuration ensures thermal reliability under deep space and lunar surface conditions, consistent with NASA’s safety and performance standards.

4.5 Propellant Transfer Validation

To evaluate internal flow performance, pressure losses, and thermal behavior of cryogenic methane through the coupler under microgravity, a CFD analysis was conducted in Ansys Fluent. The primary goal was to visualize the velocity and mass flow variations, pressure gradients, and heat transfer effects across the coupler geometry under realistic boundary conditions.

A high-fidelity 3D CAD model of the coupler was first repaired and simplified for meshing, with special attention given to the internal flow domain, including inlet and outlet sections, sealing interfaces, and the main passage geometry. A poly-hex core mesh was selected, utilizing a blend of hexahedral and polyhedral cells for optimized convergence and accuracy. Inflation layers were added to resolve near-wall viscous effects, and mesh refinement was applied at sealing zones to better capture pressure variations.

Given the low temperatures and high viscosities of cryogenics, the Reynolds number for the expected flow was sufficiently low to assume laminar behavior. Nevertheless, to ensure robust prediction of potential transitional features, the SST- $k\omega$ turbulence model was used in conjunction with the pressure-based solver. The fluid domain was defined as incompressible, with negligible density variation across the coupler.

Boundary conditions were applied to reflect microgravity conditions, with methane (CH_4) as the working fluid, entering at 100 m/s and 91 K. Simulations assumed steady-state operation, with specified inlet pressure, outlet static pressure, and a total of 100 solver iterations. Wall temperatures were held constant, and thermal conductivity for the coupler housing was included in the model.

Figure 14 shows the velocity contour plot from the final iteration. As indicated by the smooth color gradients, the flow remains stable throughout the coupler passage. Minimal recirculation or turbulent mixing was observed, confirming the effectiveness of the coupler’s internal geometry in supporting steady cryogenic fluid flow with minimal pressure loss. These results demonstrate the coupler’s ability to maintain a smooth cryogenic flow with negligible thermal or dynamic disruption.

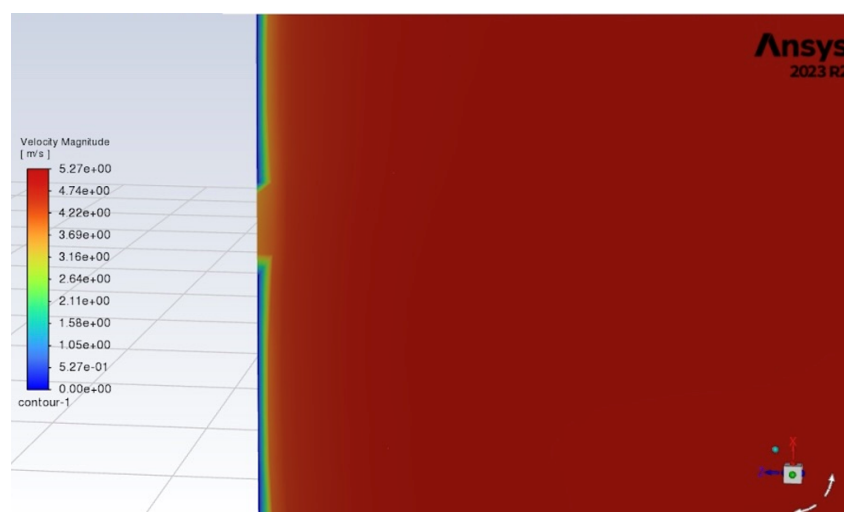


Figure 14: Velocity Contour Plot of Cryogenic Flow Through Coupler (CFD Analysis)

5 Prototype

5.1 3D Printed Model

The AMCC-AAC system was 3D printed using a Bambu Labs P1S with AMS. The 3D print was scaled down to fit a single print bed. This ensured that all problematic structural areas were easily identifiable. While an ideal prototype would consist of the full suite of AMCC-AAC's capabilities, such as the movement system and magnets, this initial realization of the design is impactful for iterating in the future. It also allows our team to physically see how the coupling process would function.



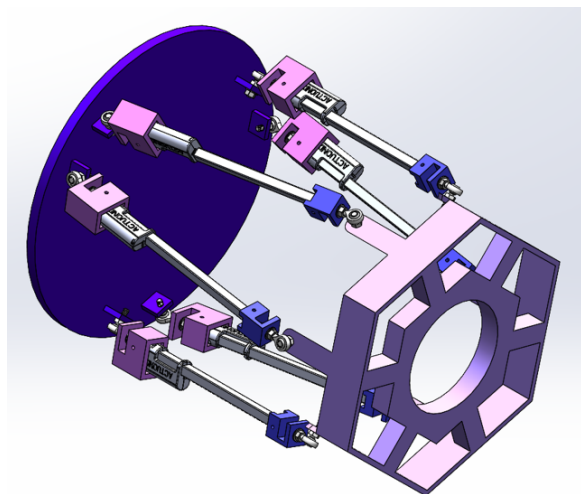
Figure 15: 3D Printed Prototype

5.2 Stewart Platform

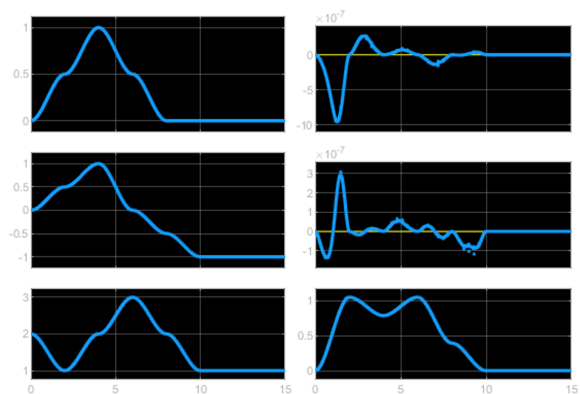
To validate the AI-guided movement system in real-world conditions, a functional prototype based on a 6-degree-of-freedom Stewart Platform was constructed. Stewart Platforms, widely recognized for their use in orbital robotics applications—including on the ISS—offer precise pose control using six linear actuators arranged in a parallel configuration [36].

The team adapted an existing student design for low-cost implementation, utilizing Actuonix linear actuators for motion and an Arduino Due for control logic [37]. A CAD model of the prototype is shown in Figure 16a. Control was achieved by solving both inverse and forward kinematics; the former is analytically derived, while the latter is numerically computed using a Newton-Raphson method [38].

The MATLAB-based controller generated actuator lengths for desired platform poses. Forward kinematic results were validated against a commanded trajectory using cubic polynomial interpolation, shown in Figure 16b. Future work will integrate live target tracking via computer vision and implement PID + feedforward control, leveraging Newton-Euler dynamics [39]. This setup enables precise coupling alignment simulations in preparation for orbital use.



(a) CAD Model of Stewart Platform Prototype



(b) Forward Kinematics Tracking Performance vs. Commanded Trajectory

Figure 16: Stewart Platform Prototype and Simulation Tracking Results

6 Technical Management

6.1 Risk Assessment and Mitigation

Once docked in space, the cryogenic coupler must operate reliably under extreme conditions, with key risks including fluid leakage, thermal contraction, propellant flow instability, and structural degradation. Even minor seal failures can lead to rapid boil-off and hazardous conditions in oxygen-rich environments. To mitigate this, helium mass spectrometry leak detection will be used for pre-deployment screening, while UHV-rated metallic seals and redundant sealing layers will help prevent failures [40]. Additionally, NASA mandates material compatibility testing to minimize flammability hazards in oxygen environments [41]. Vacuum leak testing in ANSYS Fluent will further ensure integrity against this.

Thermal contraction poses another challenge, as extreme temperature fluctuations can cause brittleness and structural stress. Materials with matched CTE will be prioritized, with titanium and stainless steel alloys offering superior low-temperature performance [41]. Cryogenic cycling tests will assess long-term durability in ANSYS Fluent [40]. Additionally, fluid behavior in microgravity can lead to cavitation and pressure spikes, requiring pressure-regulated flow control and real-time sensors to adjust transfer rates dynamically, preventing excessive buildup [42].

Structural degradation from mechanical wear and vacuum conditions must also be addressed. Low-friction coatings and wear-resistant composites will help minimize surface damage, while arc-resistant materials and electrical stress testing in ANSYS Electromagnetic Suite or MATLAB’s Partial Differential Equation Toolbox will prevent high-voltage failures [41]. By integrating these strategies, the coupler will maintain structural integrity, minimize failure risks, and ensure safe and efficient operation for long-duration space missions.

6.2 Project Timeline and Budget Estimate

To develop and validate the AMCC-AAC system up to TRL 6+, the project will follow a structured timeline spanning approximately 3.5-4 years. This includes coupler design, software development, system integration, and final validation in a relevant environment. A detailed timeline can be viewed in Figure 17 to the right. Key milestones of the project will include:

- *Year 1:* Team assembly, workspace setup, system requirements review, and initial design iterations. Low-level CFD simulations and preliminary design reviews will be conducted.
- *Year 2:* High-level system design, advanced CFD simulations, and prototyping of the coupler. Critical design review and fabrication will take place, followed by microgravity flow testing.
- *Year 3:* Software integration, AI model training, and system validation through simulated and hardware-in-the-loop testing. Pre-integration review will be conducted before final assembly.
- *Year 4:* Final system validation, microgravity testing, and software demonstration to NASA. The project will conclude with a comprehensive report and recommendations for future development.

Simulations will be the primary media used to validate the product during the early phases. In final prototype validation, the work outlined would be mostly in scaling the design to a production level

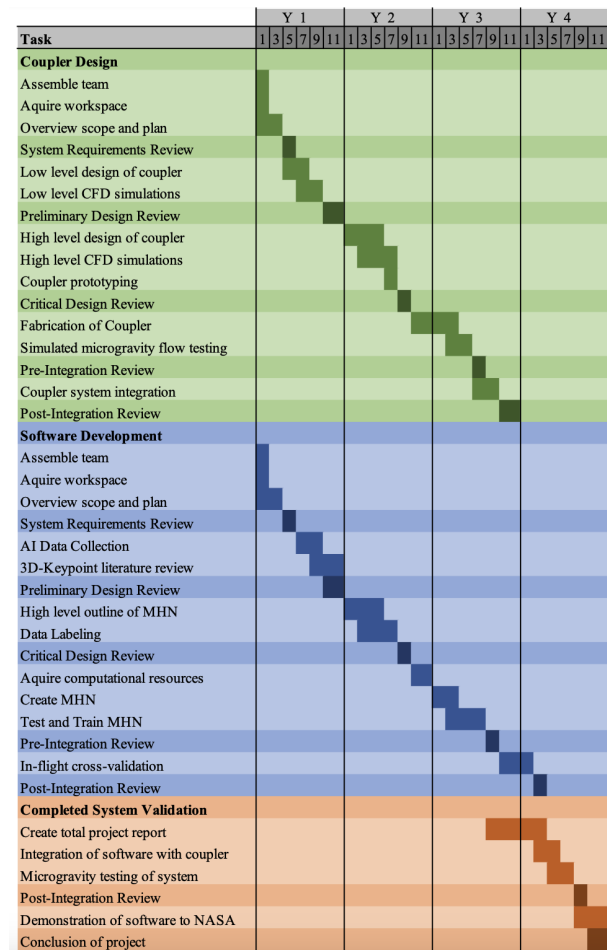


Figure 17: Full Project Timeline Overview

quality.

The project budget is structured to support the future 4 year implementation timeline, ensuring the availability of personnel, hardware, and software resources. The total estimated cost is \$6,769,156, which includes salaries, hardware, and software expenses. Major cost breakdowns include:

- *Salaries:* \$6,058,500 allocated for engineers, admins, and technicians for the project duration.
- *Hardware:* \$438,156 for coupler materials, manufacturing, sensors, and testing consumables.
- *Software:* \$272,500 for computers, MATLAB, ANSYS Fluent, SolidWorks, and cloud storage.

The following list of subteams will makeup the required domain of expertise: CAD, CFD, Manufacturing, Space Env. & Human Factors (HF), Thermodynamics, and AI/Robotics. Each subteam will have a lead project engineer, with the remaining members being junior engineers. Figure 18 illustrates the number of engineers allocated to each subteam (including leads) and their expected participation in full-time equivalent (FTE) weeks. The project will include one admin staff to manage logistics and assist with daily non-engineering tasks, as well as one technician serving in a floating role. The proposed resource distribution amounts to 3,718 FTE weeks in total. A cost margin of around ± \$500,000 was used when considering the overall cost range. Adding in this cost margin, the budget range is approximately \$6M to \$7.2M for project completion. Note that this budget is for the future 3-5 year implementation costs imposed on NASA, if the project were to commence. The proposed budget is not the costs associated with the technical paper work (i.e. the cost to manufacture a low fidelity prototype, train AI, etc.).

Category	Cost				Notes
	Amount	Unit	Unit Cost	Total Cost	
A. Salaries					
			FTE (Weeks)	FTE (Weeks)	
Project Director	1	employee	182.0	182.00	Will be required throughout project duration
CAD Engineers	3	employee	182.0	546.00	Will be required throughout project duration
CFD Engineers	2	employee	182.0	364.00	Will be required throughout project duration
Manufacturing Engineers	4	employee	182.0	728.00	Will be required throughout project duration
Space Environment/HF Specialist	1	employee	104.0	104.00	Will only be required for the 1st phase of design
Thermodynamics Engineers	2	employee	182.0	364.00	Will be required throughout project duration
AI/Robotics Engineers	3	employee	182.0	546.00	Will be required throughout project duration
Test Engineers (System Validation)	3	employee	104.0	312.00	Only needed for last 2 years of testing/validation
Software Engineers (Controls/UI)	2	employee	104.0	208.00	Needed for UI dev. For around 2 years
Administrative/Technicians	2	employee	182.0	364.00	Will be required throughout project duration
Salaries Total:	23	employees		3718.000	, total salary FTE weeks over 3.5 years
B. Hardware					
			USD (\$)	USD (\$)	
Thermal Insulation (MLI)	165	sqft	800.00	132000.00	MLI including custom fab. (20+ layers)
Coupler Materials (AlSi10Mg)	200	\$/kg	60.00	12000.00	Materials for prototyping, testing, and extra
Coupler Casing (Titanium)	70	\$/kg	400.00	28000.00	Materials for prototyping, testing, and extra
Laser Powder Bed Fusion (LPBF)	20	\$/hr	175.00	3500.00	LPBF machine and facility usage for all phases
Manufacturing Post-Processing	1	\$	1000.00	1000.00	Additional costs incurred during post-processing
LiDAR Sensors	3	\$	2000.00	6000.00	1 for prototyping, 1 for final design tests, and 1 backup
Cameras	3	\$	350.00	1050.00	1 for prototyping, 1 for final design tests, and 1 backup
Liquid Methane	100	\$/ton	400.00	40000.00	33 cycles of 2.5 min at <20kg/s (if not reused)
Liquid Oxygen	100	\$/ton	271.06	27106.00	34 cycles of 2.5 min at <20kg/s (if not reused)
Movement System (servos, robotics)	1	\$	150000.00	150000.00	Entire movement system (minus sensors & cameras)
Electronics	1	\$	35000.00	35000.00	Additional on-board chips, wiring, batteries, etc.
Miscellaneous	1	\$	2500.00	2500.00	Additional expenses like repairs/tools/etc.
Hardware Total				\$ 438,156.00	, total hardware cost over 3.5 years
C. Software					
			USD (\$)	USD (\$)	
MATLAB/Simulink	3.5	years	5000.00	17500.00	License with some add-ons required for 3 years
ANSYS Fluent	3	years	65000.00	195000.00	Enterprise CFD license for 3 years
Computers	5	computers	5000.00	25000.00	Computers required for CFD, CAD, and AI software
Additional Software/Storage Space/Etc.	1	n/a	35000.00	35000.00	Storage ~ \$30k, other softwares for AI, sensing, etc.
Software Total				\$ 272,500.00	, total software cost over 3.5 years

Total Cost (w/o salaries)	FTE (Weeks)	USD (\$)
		3718.00

Total Cost (w/ salaries)	Salaries (\$)	Total (\$)
		\$ 6,058,500.00

Estimated Salary Amounts:				
Project Director	Lead Engineer (1 per subteam)	Subteam Engineer	Administrative (1)	Technician (1)
\$ 180,000.00	\$ 140,000.00	\$ 105,000.00	\$ 78,000.00	\$ 83,000.00

Figure 18: Detailed Future Program Budget Estimate of AMCC-AAC for 3-5 Year Implementation

References

- [1] R. Patterson, A. Hammoud, and M. Elbuluk, "Assessment of Electronics for Cryogenic Space Exploration Missions," *Cryogenics*, vol. 46, no. 2, pp. 231–236, 2006, 2005 Space Cryogenics Workshop. [Online]. Available: <https://www.sciencedirect.com/science/article/pii/S0011227505001736>
- [2] "Gateway Space Station - NASA," <https://www.nasa.gov/reference/gateway-about>, 2023.
- [3] T. Kortes, "Explore Space Tech - Technology Drives Exploration," https://www.nasa.gov/wp-content/uploads/2015/03/kortes_perseverancecfm_tagged.pdf, March 2015.
- [4] T. M. Brown, M. Fazah, M. Allison, and H. Williams, "NASA Marshall Space Flight Center In-Space Cryogenic Propulsion Capabilities and Applications To Human Exploration," in *71st JAN-NAF Propulsion Meeting*, 2024.
- [5] D. Glaister, J. Schmidt, C. McLean, and G. Mills, *Long Term Cryogenic Storage Technologies Overview for NASA Exploration Applications*. [Online]. Available: <https://arc.aiaa.org/doi/abs/10.2514/6.2011-3774>
- [6] J. R. Clark, "On-orbit cryogenic refueling: Potential mission benefits, associated orbital mechanics, and fuel transfer thermodynamic modeling efforts," Master's thesis, The Ohio State University, 2021.
- [7] W. L. Johnson, N. O. Rhys, D. E. Bradley, M. Wollen, B. Kutter, M. Gravlee, and L. K. Walls, "Cryogenic orbital testbed (cryote) ground test article," NASA, Tech. Rep., 2015.
- [8] NASA, "Robotic refueling mission 3 (rrm3)," 2020. [Online]. Available: <https://www.nasa.gov/nexis/robotic-refueling-mission-3/>
- [9] "Human Landing System Requirements Document," NASA, Tech. Rep. HLS-RQMT-001, September 2019.
- [10] K. Latsyshev, N. Garzaniti, E. Crawley, and A. Golkar, "Lunar Human Landing System Architecture Tradespace Modeling," *Acta Astronautica*, 2021. [Online]. Available: <https://hdl.handle.net/1721.1/133978>
- [11] "SpaceX – Starship," <https://www.spacex.com/vehicles/starship/>.
- [12] I. Eagle Engineering, "Spacecraft Mass Estimation Relationships and Engine Data," NASA Johnson Space Center, Tech. Rep. 87-171, April 1988, prepared under NASA Contract NAS 9-17878.
- [13] N. Heersema, *Magnetically Latching Cryogenic Fluid Coupler for Lunar Surface Operations*. American Institute of Aeronautics and Astronautics, January 2024. [Online]. Available: <https://arc.aiaa.org/doi/abs/10.2514/6.2024-2371>
- [14] C. Sampaio, "Space Station Freedom Coupling Tasks: An Evaluation of Their Space Operational Compatibility," *Fourth Annual Workshop on Space Operations Applications and Research*, January 1991.
- [15] T. W. R. Justin McFatter, Karl Keiser, "NASA Docking System Block 1: NASA's New Direct Electric Docking System Supporting ISS and Future Human Space Exploration," *Aerospace Mechanisms Symposium*, May 2018.
- [16] R. F. Robbins and P. R. Ludtke, "Review of Static Seals for Cryogenic Systems," *Journal of Spacecraft and Rockets*, vol. 1, no. 3, pp. 253–259, 1964. [Online]. Available: <https://doi.org/10.2514/3.27636>

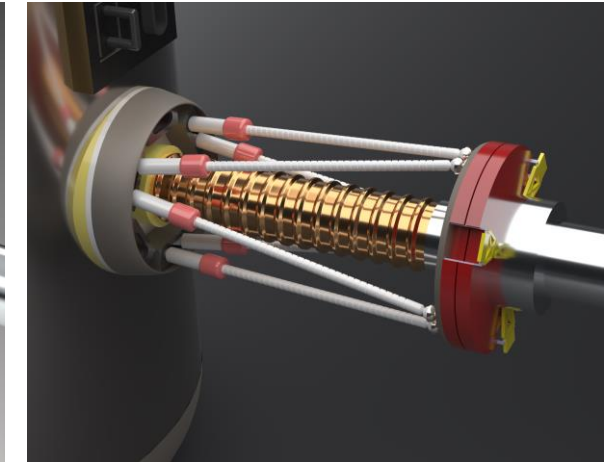
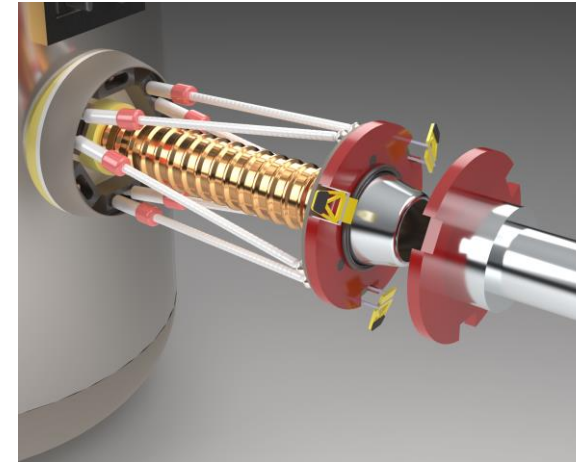
- [17] Moog Inc., “High-precision rotary actuators for space applications,” <https://www.moog.com/products/space-mechanisms/rotary-actuators.html>, 2025.
- [18] W. H. Gerstenmaier, S. Krikalev, D. Parker, G. Leclerc, and R. Shirama, “International docking system standard (idss) interface definition document (idd),” NASA, Tech. Rep., 2016.
- [19] “NASA’s Low Separation Force Quick Disconnect Device Webinar,” <https://www.youtube.com/watch?v=2hICzKjxiu0&t=1s>, June 2022.
- [20] “K&J Magnetics Force Calculator Datasheet,” https://www.kjmagnetics.com/magnet-strength-calculator.asp?srsltid=AfmBOorA_Dqe2zZNveeWZZCujDEsbwuPhavuUsBPT4-dPNKO3ITf8qsL.
- [21] R. F. ROBBINS and P. R. LUDTKE, “Review of static seals for cryogenic systems,” *Journal of Spacecraft and Rockets*, vol. 1, no. 3, pp. 253–259, 1964. [Online]. Available: <https://doi.org/10.2514/3.27636>
- [22] J. Xu, B. Song, X. Yang, and X. Nan, “An Improved Deep Keypoint Detection Network for Space Targets Pose Estimation,” *Remote Sensing*, vol. 12, p. 3857, 11 2020.
- [23] D. K. Vohra, “Optimising AI Inference for Performance and Efficiency,” 2023.
- [24] T. H. Park and S. D’Amico, “Bridging Domain Gap for Flight-Ready Spaceborne Vision,” 2024. [Online]. Available: <https://arxiv.org/abs/2409.11661>
- [25] M. Bussolino, “Multispectral Vision-Based Relative Navigation to Non-Cooperative Spacecraft,” Master’s thesis, School of Industrial and Information Engineering, Department of Aerospace Science and Technology Politecnico Milano, 2023.
- [26] “Human Landing Systems Development,” <https://www.nasa.gov/reference/human-landing-systems/>, NASA, 2023.
- [27] J. G. Santos Macías, Z. Lv, D. Tingaud, B. Bacroix, G. Pyka, C. van der Rest, L. Ryelandt, and A. Simar, “Hot isostatic pressing of laser powder bed fusion als10mg: parameter identification and mechanical properties,” *Journal of Materials Science*, vol. 57, 06 2022.
- [28] J. Rao, S. L. Sing, P. Liu, J. Wang, and H. Sohn, “Non-destructive testing of metal-based additively manufactured parts and processes: a review,” *Virtual and Physical Prototyping*, vol. 18, no. 1, p. e2266658, 2023. [Online]. Available: <https://doi.org/10.1080/17452759.2023.2266658>
- [29] C. Lapre, D. Brouczek, M. Schwentenwein, K. Neumann, N. Benson, C. R. Petersen, O. Bang, and N. M. Israelsen, “Rapid non-destructive inspection of sub-surface defects in 3d printed alumina through 30 layers with 7 μm depth resolution,” 2024. [Online]. Available: <https://arxiv.org/abs/2403.17662>
- [30] A. Thompson, D. McNally, I. Maskery, and R. K. Leach, “X-ray computed tomography and additive manufacturing in medicine: a review,” *Int. J. Metrol. Qual. Eng.*, vol. 8, p. 17, 2017. [Online]. Available: <https://doi.org/10.1051/ijmqe/2017015>
- [31] A. Ziabari, S. V. Venkatakrishnan, and Z. Snow, “Enabling rapid x-ray ct characterisation for additive manufacturing using cad models and deep learning-based reconstruction,” *NPJ Computational Materials*, vol. 9, 2023. [Online]. Available: <https://doi.org/10.1038/s41524-023-01032-5>
- [32] P. Clark, “Cubesats in Cislunar Space,” *Small Satellite Conference*, 2018.

- [33] “Quantifying mli thermal conduction in cryogenic applications from experimental data - scientific figure on researchgate,” https://www.researchgate.net/figure/Measured-data-for-performance-of-37-layer-MLI-using-double-aluminized-Mylar-DAM-and_fig1_287506453, n.d.
- [34] M. M. Finckenor and D. Dooling, “Multilayer insulation material guidelines,” NASA, Tech. Rep., 1999.
- [35] D. Corporation, “Beta cloth product page.” [Online]. Available: <https://www.dunmore.com/products/beta-cloth.html>
- [36] B. Dick, C. Oesch, and T. Rupp, “Linear actuator system for the nasa docking system,” in *European Space Mechanisms and Tribology Symposium*, 2017, available: <https://ntrs.nasa.gov/citations/20170005413>.
- [37] T. Branch, H. Liu, and D. Nguyen, “Stewart platform with electronics control and leap motion interaction,” <https://content.instructables.com/ORIG/FQC/KXUA/JIYU1JDE/FQCKXUAJIYU1JDE.pdf>, 2018, project Report, University of British Columbia.
- [38] A. Mamaghani and C. Gosselin, “Efficient computation of forward kinematics and jacobian matrix of a stewart platform-based manipulator,” in *IEEE International Conference on Robotics and Automation*, 2013, available: IEEE Xplore.
- [39] B. Dasgupta and T. Mruthyunjaya, “A newton-euler formulation for the inverse dynamics of the stewart platform manipulator,” *Mechanism and Machine Theory*, vol. 33, no. 8, pp. 1135–1152, 1998.
- [40] “Standard Test Method for Calibration and Operation of the Falex Block-on-Ring Friction and Wear Testing Machine,” vol. 05.01, no. D2714-94R19, p. 4, 2024.
- [41] “Standard Materials and Processes Requirements for Spacecraft,” NASA, Tech. Rep. NASA-STD-6016A, 2016.
- [42] M. hee Kim, J. Wilson, F. Cucinotta, L. Simonsen, W. Atwell, F. Badavi, and J. Miller, “Contribution of High Charge and Energy (HZE) Ions During Solar-Particle Event of September 29, 1989,” NASA, 07 1999.

Major Objectives & Technical Approach

- Enable autonomous magnetized propellant coupling using a robotic active alignment system
- Employ data training sets for real-time computer vision (RCV) docking system
- Perform system cross-checks using on-board sensors to minimize need for human interaction
- Develop a quick-disconnect system to improve safety of astronauts aboard HLS during a system failure

Image/Graphic:



Key Design Details & Innovations of the Concept

- Utilizes existing HLS sensors as well as LiDAR and cameras for inputs to the RCV active alignment control system
- Implements magnetized cryo-coupler with a 6 DOF robotic movement system for maximum performance alignment
- Compressive robotic grippers (yellow) improve suction forces on couplers ensuring minimal leakage
- Multi-layer insulation (MLI) reduces boil-off effects and heat flux from cryo-coupler system
- Laser Powder Bed Fusion (LPBF) is used as an additive manufacturing technique to create complex coupler geometries with extreme precision

Summary of Schedule & Costs for the proposed solution's path to adoption

- 4-year schedule to finalize model architecture, gather training data, fabricate coupler, and complete integration testing.
- Multiple subteams working simultaneously to reduce length of project and to ensure proper integration between ML model and mechanical coupler system
- Total budget is around \$6.7M which accounts for all salaries, hardware, and software needed

Budget Breakdown

